



PerTPV – Perovskite thin film photovoltaics
Grant agreement 763977

Deliverable 2.6

Report of loss mechanisms in various diode architectures as a function of processing and device stressing

WP2

Lead beneficiary: [IIT]

Authors: [Annamaria Petrozza, Yang Zhou, Suhas Mahesh, Henry Snaith]

Delivery date: [31/03/2021]

Confidentiality level: [Public]



The PerTPV project has received funding from the European Union's Horizon 2020 research and innovation programme under grant agreement No 763977.

Revision History

Author Name, Partner short name	Description	Date
Annamaria Petrozza	Draft deliverable	25/02/2020
Suhas Mahesh & Henry Snaith	Revision 1	30/03/2021
Henry Snaith	Final version	01/04/2021

REVISION HISTORY	2
1 INTRODUCTION.....	3
2 PRISTINE PEROVSKITE THIN FILM.....	3
2.1 MAPBI3 (BANDGAP, EG ~ 1,65EV).	3
2.2 WIDE BAND GAP PEROVSKITES – MIX HALIDE (EG ~ 1,8EV-1,7EV).	6
2.3. 3D PEROVSKITE WITH LARGE ORGANIC CATION.....	7
3 INTERFACE PEROVSKITE THIN FILM/CHARGE EXTRACTING LAYER (CEL)	12
3.1 PCBM.	12
3.2 PEO.	13
4 WIDE BAND GAP PEROVSKITE – QUANTIFYING OPEN-CIRCUIT VOLTAGE LOSS.....	14
5 CONCLUSIONS.....	25

1 Introduction

Within Task 2.3, we have focused our researches on the understanding of the physical and chemical processes occurring in the complete solar cell in order to eventually understand how losses are induced. We have started from the investigation of losses in pristine thin films, then we have extended the investigation to perovskite layers interfaced to charge extracting layers according to the main devices architectures used within the Network.

2 Pristine perovskite thin film

2.1 MAPbI₃ (bandgap, $E_g \sim 1,65\text{eV}$).

By combining photoluminescence measurements under controlled conditions with ab initio simulations we reveal for the first time that photo-instabilities are related to both light-induced formation and annihilation of defects acting as carrier trap states. These phenomena coexist and compete. We define characteristic length and time scales and the experimental conditions responsible for both processes. We show that short length and time scale defect annihilation can prevail over defect formation, occurring on longer scales, when effectively blocking under-coordinated surface sites, which act as a defect reservoir. By an effective surface passivation strategy we are thus able to stabilize the perovskite layer towards such photo-induced instabilities, leading to improved optoelectronic material quality and enhanced photo-stability in a working solar cell. We monitored the PL intensity of MAPbI₃ and MAPbBr₃ perovskite thin-films used in efficient solar cell devices as a function of illumination time. Figure 1a shows the room temperature integrated PL over time of MAPbI₃ polycrystalline films deposited on glass. The sample was excited with a laser beam incident on the film surface. The laser was modulated with a fixed pulse width of 200 ns (fluence per pulse $\square 1\mu\text{J}/\text{cm}^2$) and varying repetition rate, i.e. varying the period (δ) between two excitation pulses. To exclude the effect of oxygen and moisture all measurements were performed under active vacuum (pressure $<10^{-5}$ mbar, under constantly running pump). We observe that the PL intensity changes over time, showing both PLE and PLD, depending on the repetition rate for both MAPbI₃ and MAPbBr₃ (Figures 1a,c). At low repetition rates -that is long δ , corresponding to the sample being in the dark for $\square\text{ms}$ time – the PL intensity cumulatively grows with subsequent illumination periods. Increasing the repetition rate - short δ , corresponding to longer light exposure and less time in the dark- a quenching process kicks in which becomes eventually dominant (Figures 1a,c). These observations clearly indicate that light absorption can lead to competing PLE and PLD phenomena, depending on the excitation conditions. We thus performed additional experiments at varying temperatures to disentangle the factors underlying the individual phenomena involved in PLE and PLD. Figure 1b shows the time evolution of the integrated PL intensity of a MAPbI₃ film excited with continuous-wave (CW) light, analogous to a very high repetition rate, i.e. short δ , at different temperatures. Each curve was taken on a fresh spot of the sample. For MAPbI₃, at 77 K the PL is stable for the entire duration of the experiment, and the same holds when heating the sample to 137 K. Further raising the temperature to 197 K we observe a strong PLE over time which is further boosted up to 237 K, leading to a factor of $\square 8$ PL increase compared to the initial value. At still

higher temperature (277 K) an initial PLE is superseded by PLD at longer exposure times, which eventually dominates at room temperature and above. Similar behavior was observed for MAPbBr₃ films upon varying the temperature, though with lower thresholds for PLD and PLE (Figure 1c,d). The PL intensity variations with increasing temperature and the transition from stable PL, to PLE to PLD, is clearly suggestive of competing thermally activated processes that either improve or hinder the efficiency of radiative recombination. The dominant contribution of PLD at higher temperature suggests a higher energy demand for this process compared to PLE. Also, the enhanced stability range of MAPbI₃ compared to MAPbBr₃ at low temperatures (cf. Figure 1b and 1d, with PLD starting at 277K and 197 K respectively) suggests that the threshold for switching between the two phenomena is determined by the precise material composition, in particular by the nature of the halide. The time scales involved in PLD and PLE are consistent with the reported ionic activities, such as ion/defect annihilation and migration rates, in both MAPbI₃ and MAPbBr₃ and with the time scale of photo-induced transformations in free standing MAPbI₃ films. Comparably, in mixed halide (I, Br) perovskites ion segregation was shown to take place via halide defects, mainly vacancies and interstitials, driven by the gradient in carrier generation through the thickness of these strongly absorbing materials. The observation of typical spectral features associated with defects in the lattice that are enhanced under illumination (Fig 2) is suggestive of photo-induced defect formation and annihilation being respectively related to PLD and PLE. The PLD process is likely more complex than PLE. We know that PLD is favored by high illumination repetition rates. This is in turn associated with a larger fraction of traps being filled at any time, and possibly to a higher effective temperature due to heating of the sample. We also know from the wavelength dependence of PLD that this process is more efficient when the photo-generation happens close to the surface where a larger trap density can be envisaged. It is also amplified when ion diffusion is enhanced, i.e. by the presence of gradient across dark/light regions. A possible PLD mechanism could thus be reasonably associated to a bimolecular reaction – boosted by increasing the encountering probability of the reactants, i.e. by increasing their density and/or their mobility – occurring among the filled, long living traps, in a film region close to the surface. We have identified interstitial halides (e.g. I⁻) has those point defects able to introduce deep charge trapping states (see Motti et al, *Advanced Materials* 31 (47), 1901183). Following the initiating trap filling reaction, two filled traps could react to form an I₂ molecule. Consistently, I₂ loss into toluene solution following MAPbI₃ light irradiation has been measured. I₂ can be trapped as a complex in the bulk or it may disproportionate to reform the li⁺/ li⁻ interstitial pair. Importantly, both coordinated I₂ and the li⁺/ li⁻ pair tend to migrate to the surface, being stabilized by 0.4 eV. A surface-coordinated I₂ molecule represents the final reaction product. Such I₂ molecule can remain bound to the surface or to grain boundaries. Notably I₂ can act as an electron trap, as li⁺ does. The iodine imbalance between surface and bulk can trigger a series of compensating reactions that regenerate the starting equilibrium distribution of li⁺/ li⁻ defects to compensate their transformation to surface bound I₂. This process leads to an enhancement of charge trapping states first (Fig 2.a), to the degradation of the thin film over time.

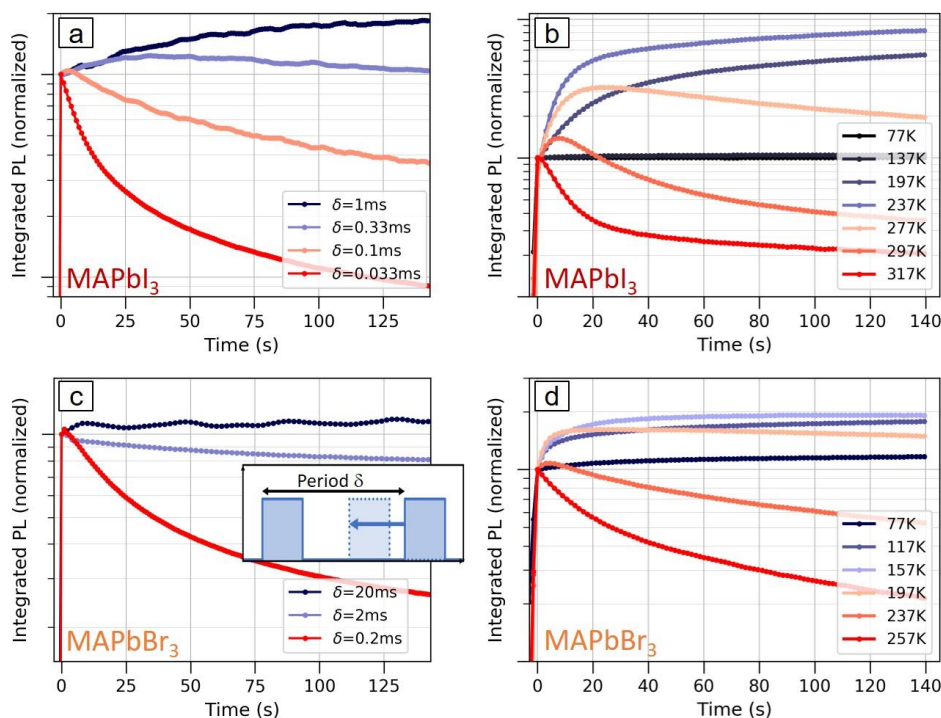


Figure 1: Integrated PL intensity over time under illumination (fluence $\sim 0.5 \mu\text{J cm}^{-2}$, excitation density $\sim 10^{16} \text{ cm}^{-3}$) on fresh spots of polycrystalline films of MAPbI₃ (a) and MAPbBr₃ (c) with increasing repetition rate (decreasing period) of the excitation light. The pulse width was fixed at 200 ns for MAPbI₃ and 10 μs for MAPbBr₃ (200 ns pulse with is shown in Fig S5). Integrated PL over time of MAPbI₃ (b) and MAPbBr₃ (d) at different temperatures under CW excitation. Excitation wavelength: 450 nm for MAPbI₃ and 405nm for MAPbBr₃.

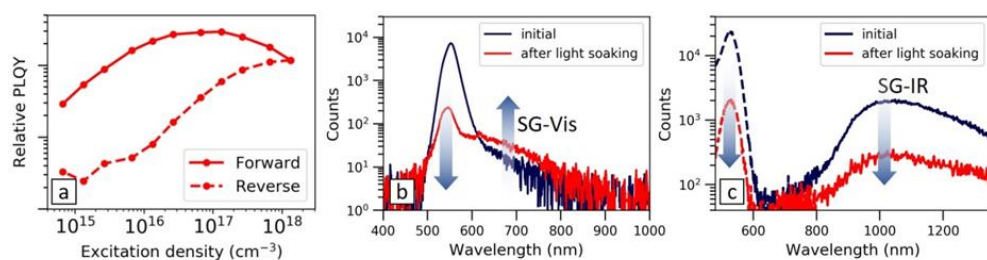


Figure 2: a) Relative PLQY curves of a MAPbBr₃ thin film taken in vacuum with increasing (solid lines) or decreasing (dashed lines) excitation densities; PL spectra of MAPbBr₃ thin films taken with b) a detector sensitive to visible light and c) an infrared sensitive detector, before and after prolonged illumination (approximately 40 minutes, 250 kHz, at excitation density around 10^{16} cm^{-3}). The emissive band centered around 680 nm has been assigned to the radiative recombination of holes at I⁻ (negatively charged Iodine interstitial) and the emissive band centered around 1100 nm has been assigned to the radiative recombination of electrons at I⁺ (positively charged Iodine interstitial), ref to: Motti et al, Advanced Materials 31 (47), 1901183.

2.2 Wide Band Gap Perovskites – Mix Halide ($E_g \sim 1,8\text{eV}$ - $1,7\text{eV}$).

In Figure 3 we summarize possible origins of V_{oc} losses in wide bandgap perovskite solar cells. Together with thin film interfacial defects, the presence of inter-grain defects and bulk defects, whether they introduce deep charge trapping states or not, induce a secondary and detrimental effect which is the segregation of low band gap semiconducting phases upon light soaking induced ion migration which eventually result in a further reduction of the V_{oc} . Here we report about possible strategies, which target an improvement of the optoelectronic quality of the perovskite thin film. Halides commonly take the crystal boundaries and, more generally crystal defects, as migration pathway, which means halide segregation can also be reduced by improving crystallinity.

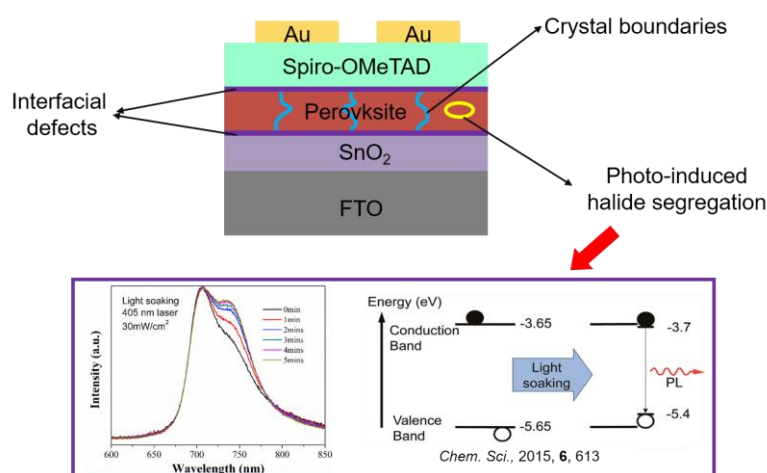


Figure 3: Sketches representing possible losses in wide bandgap perovskite solar cells

First, it has been demonstrated that the use of a designed solution containing $\text{Pb}(\text{SCN})_2$ ($(\text{CsI})_{0.15}(\text{FAI})_{0.85}[\text{Pb}(\text{SCN})_2+2\text{FAI}]_x[\text{Pb}(\text{SCN})_2+2\text{FABr}]_{1-x}$, Solution B) to add into parents solution ($(\text{CsI})_{0.15}(\text{FAI})_{0.85}(\text{PbI}_2)_x(\text{PbBr}_2)_{1-x}$ Solution A), can highly improve the crystallinity of wide bandgap perovskite and maintain its stoichiometry. Based on the highly crystallized sample prepared by mixture of solution A and B, we further modified the composition and crystallinity by adding $(\text{CsI})_{0.15}(\text{GAI})_{0.85}(\text{PbI}_2)_{0.25}(\text{PbBr}_2)_{0.75}$, Solution C, which contains guanidinium (GA). Here we take the wide bandgap perovskite of $\text{Cs}_{0.15}\text{FA}_{0.85}\text{PbI}_{1.5}\text{Br}_{1.5}$ as a model system, which has the optimal bandgap (1.86eV) to be the top absorber in perovskite/perovskite tandem. The samples prepared with mixture of A and B will denoted as W/O GA, while the sample prepared with mixture of A, B and C will denoted as W/ GA. In Figure 4 we show that the presence of GA improves the thin film crystallinity (Fig 4.a) and at the same time reduce the formation of a I rich phase upon illumination (Fig 4.b and Fig 4.c). We finally test the use of GA also as surface passivating molecules. In Figure 5 we present the figure of merit of solar cells to show cooperative effect of GA to improve the bulk and surface quality of the thin film.

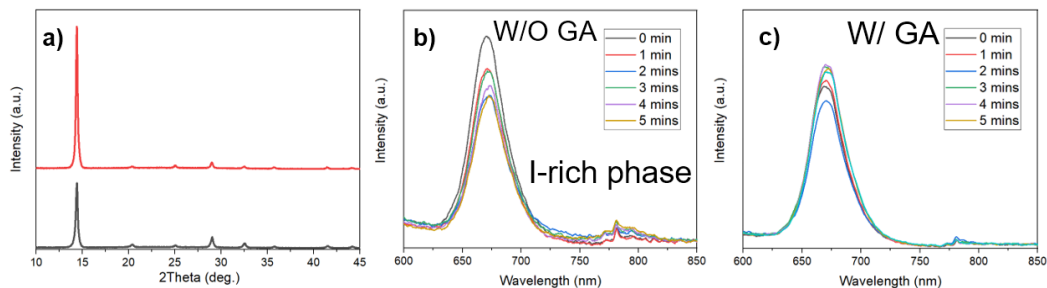


Figure 4: a) XRD patterns of samples prepared W/O GA (black), and W/ GA (red); Photoluminescence spectra of thin films b)W/O GA and c) W/GA.

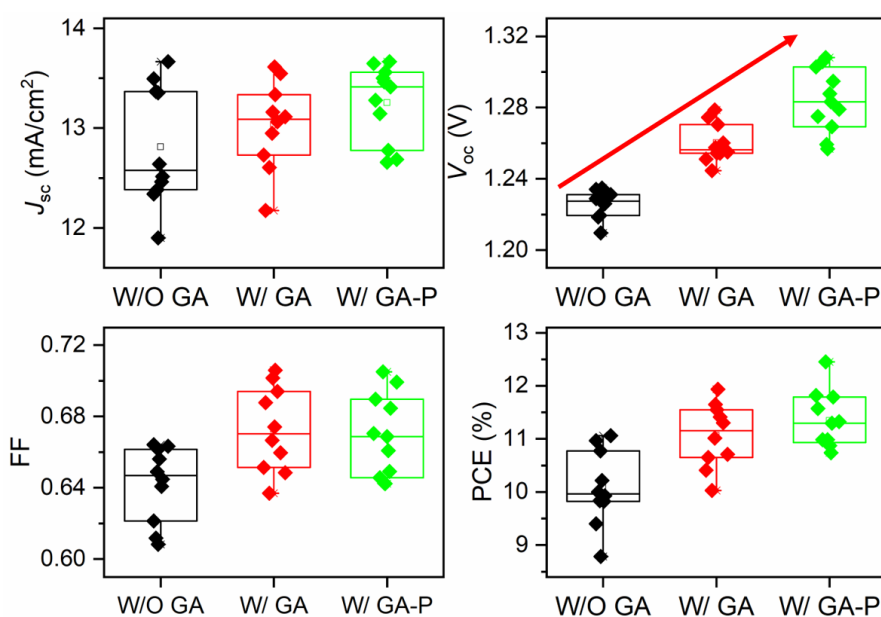


Figure 5: figures of merit of solar cells to show cooperative effect of GA to improve the bulk (w/GA) and surface quality (W/GA-P) of the thin film.

2.3. 3D Perovskite with large organic cation.

We investigate how bulky organic cations, which have an ammonium group and different alkyl lengths, incorporate in multi-dimensional perovskite phase and affect perovskite solar cells in terms of PV properties and device stability. In particular, we compare ethyl ammonium (EA) and butyl ammonium (BA) ions. The BA cation has been used to produce 2D/3D perovskite structures, but there has been a broad statistic of PCEs depending on the chemical composition and processing methods of the thin films. The EA, present the same functional groups and it simpler smaller. It has been reported as surface passivation molecule and directly within multication 3D perovskites. Nevertheless, the conditions which determine how this molecule should be used need to be studied thoroughly yet. We focus on these two cations to investigate how they will be integrated within the perovskite thin film in terms of structural and morphological properties and then how this affects the optoelectronic properties and stability upon

stimuli of the thin film and the relative solar cells. As a control system, we used formamidinium (FA) and cesium (Cs) as A-site cations to form the 3D perovskite phase. The FACs perovskite, with a mole ratio of FA:Cs = 0.85:0.15, has been reported to display high efficiency solar cells with an average PCE around 17%. We added these large cations into 3D-forming perovskite solution, composed of FA and Cs ($\text{FA}_{0.85}\text{Cs}_{0.15}\text{PbX}_3$ with $\text{X} = \text{I}_{0.9}\text{Br}_{0.1}$), and then we grew the polycrystalline thin film by using a conventional solvent-quench method. The perovskite films were sandwiched between SnO_2/PCBM and spiro-OMeTAD for standard single-junction device configuration. We started investigating how changing the mole fraction of EA-mixed and BA-mixed perovskite could affect the PV performance. We incorporated the bulky cation into $\text{FA}_{0.85}\text{Cs}_{0.15}\text{Pb}(\text{I}_{0.9}\text{Br}_{0.1})_3$ perovskite precursor, ensuring the desired stoichiometry in the resultant films. Figure 6a shows the average PV parameters obtained from 24 identical devices for each system. In the case of the EA-FACs devices, the PV statistics show an obviously increasing trend for PCE from $x = 3$ to 10%. Then, when the EA composition reaches 20% or above, the device shows a decrease in PCE. This trend reflects all the PV parameters such as open circuit voltage (V_{oc}), short circuit current density (J_{sc}), and fill factors (FF). On the other hand, the BA-FACs devices show a continuous decrease in all of the figures of merit as increasing the BA composition. Thus we have chosen 10% concentration of the cation to further advance our investigations. The control FACs perovskite exhibits a V_{oc} of 1.08 V, a J_{sc} of 20.5 mA cm^{-2} , and a FF of 0.72, yielding an average PCE of 16.2%. The device employing EA10%-FACs perovskite film achieves higher V_{oc} of 1.11 V, a J_{sc} of 21.2 mA cm^{-2} , and an FF of 0.76, leading to an improved PCE of 17.9%. However, the BA10%-FACs device exhibits an inferior performance with lower PV parameters: a V_{oc} of 0.94 V, a J_{sc} of 17.6 mA cm^{-2} , and an FF of 0.55. Figure 6d shows the corresponding EQE spectra for the best PV device for each cation. The EQE of the EA-FACs device has a higher average value in the wavelength range from 300 to 800 nm compared to the control and BA-FACs. All of the integrated J_{sc} values from the three devices are well-matched with the values from the J–V results. The reduced J_{sc} and V_{oc} of BA10%-FACs are closely related to charge recombination processes in the device. First, we measured J_{sc} under different light intensities (I) ranging from 5 to 100 mW cm^{-2} (Fig. 6e). J_{sc} goes $\propto I^\alpha$, where α should be close to 1 if the devices have sufficient electron and hole mobilities and no space charge effects. The fitted α values are 0.994, 0.998, and 0.964 for the control FACs, the EA-FACs, and BA-FACs, respectively. The BA-FACs device shows a stronger deviation from the unity of slope, which might be related to stronger charge recombination than the control and EA-FACs. We also measured V_{oc} at different I (Fig. 6f). V_{oc} depends logarithmically on I with a pre-factor, the so-called diode ideality factor n_{id} , which can be determined from a measurement of V_{oc} as a function of I : $V_{oc} = \frac{E_g}{q} - (n_{id} kT)/q \ln\left(\frac{I_0}{I}\right)$ with E_g the band gap energy, n_{id} the ideality factor, k the Boltzmann constant, T the temperature, q is the elementary charge, and I_0 is a constant with the same unit as I . The FACs and EA-FACs devices show $n_{id} = 1.62$, which is reasonably in agreement with the reported values ranging from 1.6 to 1.8 in the previous papers. It is associated to Shockley-Read-Hall recombination processes in the bulk of a mostly intrinsic perovskite film. On the other hand, the BA-FACs device shows n_{id} of 1.44 together with lower V_{oc} values than 1 V. This low n_{id} along with a low V_{oc} might indicate strong surface recombination in PV devices, which has been observed for perovskite solar cells with an energy-level-unmatched electrode or without hole transporting layer. XRD patterns were

measured to understand the arrangement of large cations in the 2D/3D perovskite structure (Fig. 7). The control FACs perovskite shows typical diffraction profiles of 3D perovskite phase which has a (110) diffraction peak at 14.05° . The diffraction profiles of the EA5%- and EA10%-FACs perovskite films show similar diffraction peaks to the control FACs perovskite but with a slight shift of the (110) diffraction peak toward smaller angle at 14.0° without low n phase perovskite formation. Considering the ionic size of the EA cation that is slightly larger than FA, we can assume that EA is compatible with a 3D structure, placing in “quasi-3D” structure. Thus, we suggest that an EA amounts as small as 10% can still form a 3D perovskite phase with a slight lattice expansion. Interestingly, the EA5%- and EA10%-FACs films show stronger (110), (220), and (310) diffraction peaks from 3D perovskite phase than the FACs film, which indicates that EA addition of 5 - 10% induces higher crystallinity of perovskite film (Fig. 7c). Beyond $x = 0.2$, $\text{EA}_x(\text{FACs})_{1-x}$ starts to show a diffraction peak from the low dimensional phase in the perovskite film at the peak of 8° (corresponding to $n = 2$). The diffraction scan of the EA50%-FACs shows the $n = 1$ diffraction peak, located at 11.7° , and a weakened (110) diffraction peak from 3D perovskite phase. The d -spacing from the $n = 1$ diffraction peak is 11.1 \AA , which corresponds to the (020) plane with a stack of EA spacers. On the other hand, the BA-FACs perovskite shows a $n = 2$ diffraction peak at 4.5° already from the BA composition of 10% (Fig. 7b). Due to the large size of BA cation, it does not incorporate into 3D perovskite phase at all, but it forms a 2D perovskite phase. The $n = 2$ diffraction peak comes from (020) plane, reflection at 4.5° is observed for the BA-FACs film, which corresponds to the (020) crystal plane of the 2D perovskite phase. The BA-FACs films display similar or slightly weaker (110), (220), and (310) diffraction peaks from 3D perovskite phase, compared to the FACs control (Fig. 7d). As increasing BA composition, diffraction peaks from low-dimensional perovskite phase become prominent until 50%. In the case of BA100% perovskite, it exhibits $n = 1$ diffraction peak at 5.8° . To elucidate where the bulky cation locates in the 2D/3D perovskite films, we measured dynamic secondary ion mass spectrometry (DSIMS) and obtained depth profile of ionic species coming from the perovskite film under the Cs^+ ionic sputtering. The control FACs perovskite film shows a homogeneous distribution of every component including Pb, CN_2 ion, and I ion along with the depth profile (Fig. 7a). The EA10%-FACs perovskite also exhibits a similar depth profile except a small bump locating an accumulation of CN_2 at the buried interface (Fig. 7b). Discerning FA (CH_5N_2 , MW = 172) and EA ($\text{C}_2\text{H}_8\text{N}$, MW = 173) cations is difficult since they have similar molecular weights. However, it has been reported by previous works that bulky cations in 2D/3D perovskites are likely to accumulate at buried interface.^{42, 43} In agreement, XPS measurement shows an identical surface chemical composition of EA-FACs and FACs film (Table S1). In the case of the BA10%-FACs film, the depth profile displays a strong peak of carbon signal at the buried interface with a thickness around 150 nm, which can be definitely differentiated from the CN_2 curve that already shows a substantial decrease at the buried interface (Fig. 7c). This carbon accumulation comes from the BA cation that has three more carbons than FA. Such vertical distribution is also confirmed by the detection of photoluminescence spectra from the top and buried perovskite surface (data not shown). In Fig. 8 we present a schematic drawing which summarizes the thin film morphology evolution upon doping with large organic cations. Up to 10% load with the EA cation, the molecule remains disperse within the 3D phase and at the bottom without forming a 2D perovskite phase. Only above 10% of the EA cation concentration 2D

crystalline phases start forming. Most importantly, the incorporation of EA induces a smooth, compact, and large-size perovskite crystal formation as confirmed by XRD and SEM measurements (data not shown). This also results in a lower defect density and enhanced PL emission with respect to the control sample. Above 20% EA mole fraction, perovskite starts to form $n = 2$ phase layer at the buried interface, and the thin film morphology also shows smaller grains. By introducing a novel molecular descriptor for larger molecular cations, the “globularity factor” (i.e., the discrepancy of the molecular shape and an ideal sphere), it was shown that EA may be a suitable candidate for multi-cation 3D perovskites. MA/EA perovskite solar cells with very large EA loading were characterized²⁵. However, here it is clear that different cations combinations, i.e. the addition of FA/Cs, can affect the stabilization and of single components within the structure and the thin film morphology at different loads. On the other hand, even with a small amount of BA addition, the perovskite thin film shows $n = 2$ phase formation and a much rough surface morphology with small perovskite grains. The inclusion of BA in 3D perovskite phase induces strong vertical segregation and large volume expansion, which substantially affects 2D/3D film formation. Though the film still shows good emissive properties, this segregation will act as a barrier for charge transport and collection to the electrode and induces surface recombination, as shown in Fig 6.

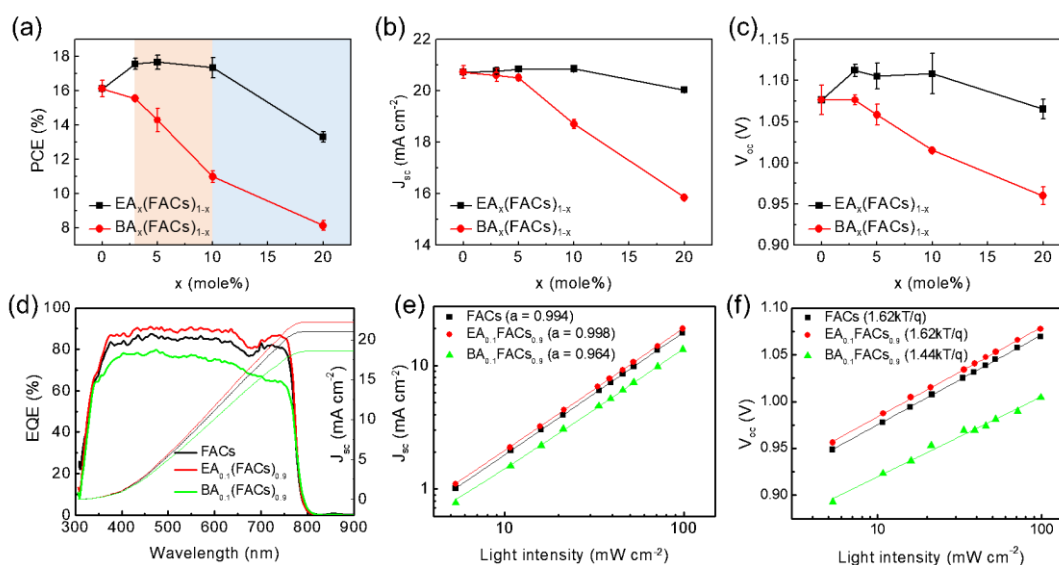


Figure 6: (a, b, c) Photovoltaic parameters determined from the J - V characteristic of the perovskite solar cells prepared with $EA_x(FACs)_{1-x}$ or $BA_x(FACs)_{1-x}$ as a function of mole fraction, x ($FACs = FA_{0.85}Cs_{0.15}Pb(I_{0.9}Br_{0.1})_3$). (d) EQE spectra of the photovoltaic devices. (e, f) J_{sc} and V_{oc} as a function of light intensity.

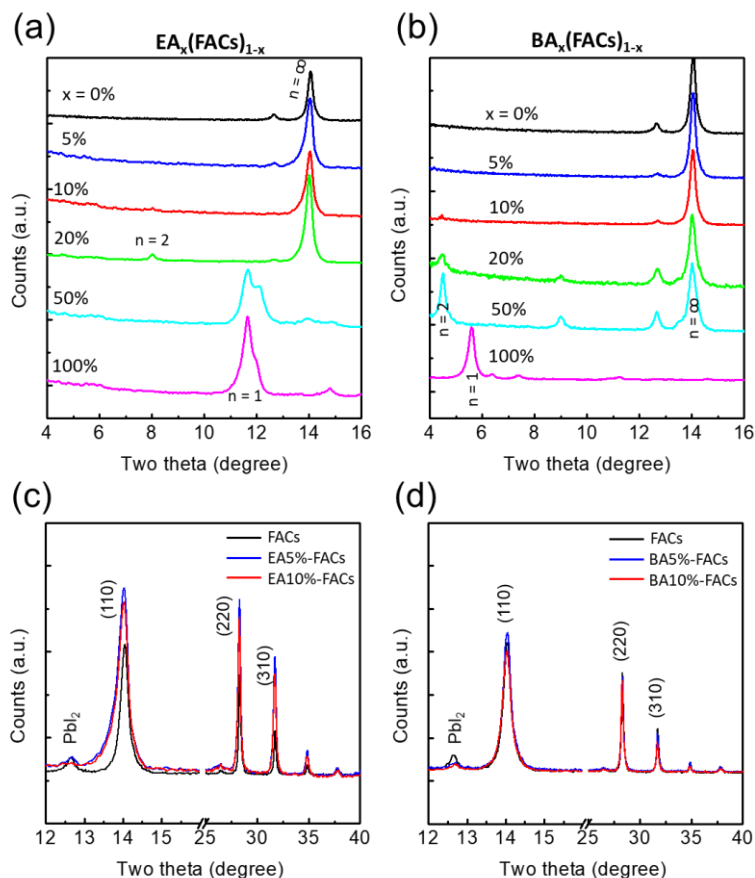


Figure 7: XRD patterns of EA (a,c) and BA (b,d) 2D/3D perovskite structure

To gain insight into the operational stability of the mixed 2D/3D perovskite solar cells, maximum power point (MPP) of PV device was tracked under 1 sun illumination (UV spectrum included) for 60 h in a way of simulating day and night cycle for 12-h illumination and overnight storages (Fig. 8a). We compared the control FACs, EA10%-FACs, and BA10%-FACs devices. This cycling test monitors not only the device operational stability but also the recovering property in the dark.⁴⁶ The devices were measured in ambient condition at a relative humidity of 40 ~ 70% without encapsulations. The power conversion efficiency of the EA10%-FACs device is stable at 17% over the entire probing period. The control FACs and BA10%-FACs devices show a stark contrast to the EA10%-FACs. For the 1st-day stability test, they do not show any decrease in PCE similar to the EA-FACs device, but on the 2nd day, it exhibits an apparent decay in MPP by 20%. In addition, on the third day, even though the PCE recovers back of its initial PCE, it rapidly decays to 40% of the PCE over the 12-h illumination. The BA-FACs device also exhibits a similar trend to the control FACs device. Especially, on the third day of illumination, it obviously shows a decay in PCE during the testing process by 40%.

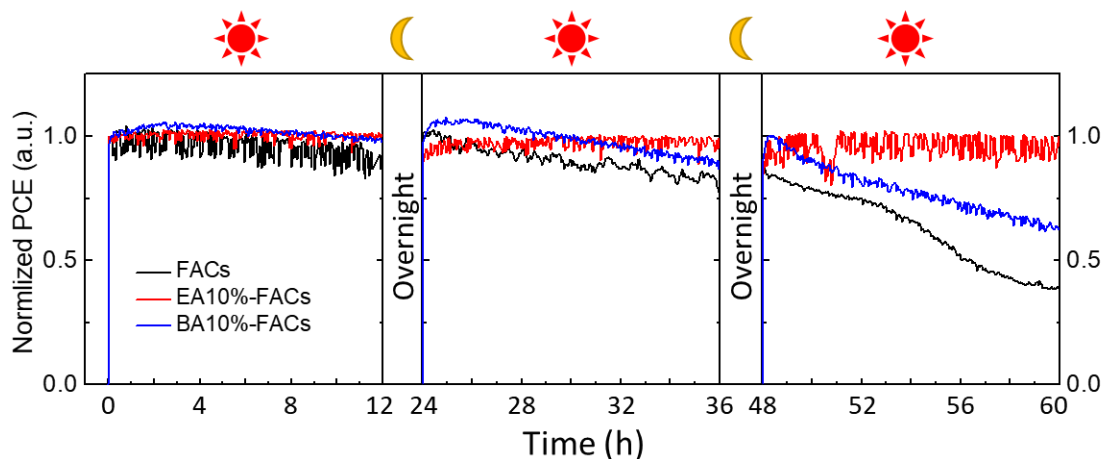


Figure 8: operational stability tests without encapsulation by tracking at their maximum power points under 1-sun illumination by xenon lamp. RH 40% -70%

3 Interface perovskite thin film/charge extracting layer (CEL)

In section 2.1 we show that I₂ can be formed in MAPBI₃ upon continuous illumination. Now we want to understand what happen when the perovskite is interfaced with other materials.

3.1 PCBM.

When exposed to I₂ vapour the PCBM thin film results n doped. This process can be monitored by looking at the 1460 cm⁻¹ Raman mode, which shift upon doping (Fig 9). We monitor the same mode while illuminating a perovskite thin film, with on a topo a thin layer of PCBM and we observe the same trend as when exposing the PCBM thin film to I₂ vapours. This suggests that PCBM is not able to hamper the I₂.

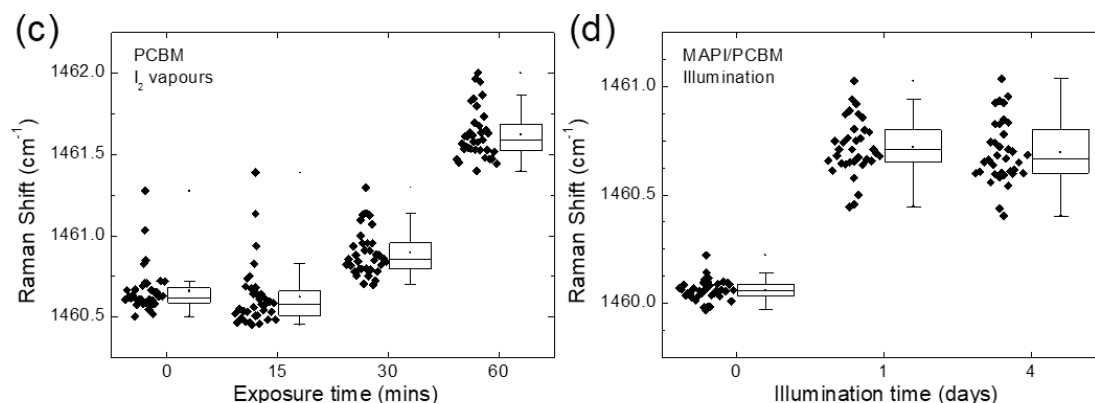


Figure 9: Monitoring the shift of the Raman more at 1460 cm⁻¹ upon light soaking of PCBM only (a) and MAPI₃/PCBM bi-layer (b)

3.2 PEO.

We compared a pristine MAPbI₃ film with one coated with tri-n-octylphosphine oxide (TOPO) or polyethylene oxide (PEO) (Figure 10a). TOPO has been applied for the passivation of perovskite films resulting in enhanced PL efficiencies and lifetimes. PEO is a polymer containing polar ether groups and hydroxyl terminations, representing a moisture barrier and a possible passivating agent (ref Energy Environ. Sci., 2018,11, 2609-2619). In Figure 10.a, by illuminating a fresh spot of the samples (560 nm, CW excitation, fluence of $\sim 0.1 \mu\text{Jcm}^{-2}$) and monitoring the integrated PL signal over a few minutes we observed a slow quenching for the bare MAPbI₃ thin film and an initial enhancement followed by a slower quenching for the TOPO passivated thin film. On the other hand, in the presence of PEO we observe that the mechanism leading to PLID is switched off even at room temperature (Figure 10.b). Despite TOPO and PEO are both characterized by the presence of oxygen atoms which interact with undercoordinated surface Pb atoms, the increased PL observed with PEO is suggestive of a more effective passivation by the latter, probably because of the larger fraction of oxygen atoms against aliphatic carbon chains in PEO. Figure 10.b shows the relative PL quantum yield, calculated as the integrated PL intensity normalized by the excitation intensity, of MAPbI₃ films. Each data point was taken after a hold time of ~ 30 seconds. When measuring from low to high excitation intensities (solid lines) and then in reverse order (dashed lines), we observe a hysteretic behavior resulting from photoinduced trap formation, i.e. PLID and a concomitant PL intensity reduction from bare perovskite thin films. By illuminating the film from the passivated side, both the TOPO and PEO coated samples show a higher PL signal, indicating a decrease in the density of native defects on the thin film surface. Thus, also in agreement with the data shown in Figure 4a, the sample coated with TOPO shows a less pronounced hysteretic behavior compared to the uncoated film, while the PEO passivated thin film presents an opposite hysteretic behavior of the relative PL as a function of excitation intensity, as a consequence of a dominant PL enhancement process. This clearly shows that efficient surface passivation can reduce the density of defect states and photo-stabilize the perovskite thin film. The passivating PEO layer has a significant technological relevance as it allows for the formation of high quality interlayer thin films which can be easily implemented in perovskite solar cells. In Figure 4c we show the J-V characteristic of MAPbI₃ based solar cells. Here we add PEO interlayers between the perovskite active layer and the selective charge extracting layers. The PEO layer is seen to improve the open circuit voltage (VOC) when applied to either the electron- or hole-extracting interface, with the best performance given by the device with PEO applied to both sides. In Figure 10.d we show the evolution of the VOC of solar cells with and without the PEO interlayers under one sun illumination. The devices were encapsulated in inert atmosphere. Despite the fact that the perovskite layer in the reference device is already interfaced with materials which have, to some extent a passivating role, such as C60, We still see competing dynamics in the Voc which mirror the PL enhancement and decrease shown in Figure 10.a. However, the relative contribution of the PL reduction is drastically reduced in the PEO-treated device, resulting in a higher and more stable Voc. These results suggest that a good passivation of the uncoordinated Pb atoms on the thin film surface avoids the I₂ loss.

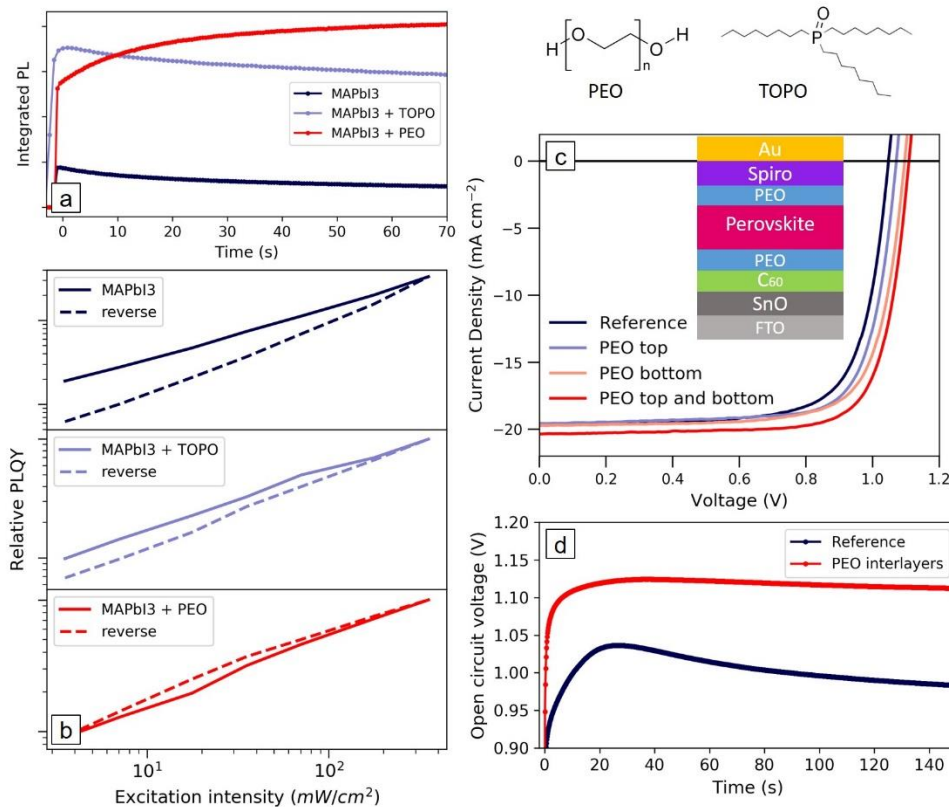


Figure 10: PL intensity over time of the MAPbI_3 films bare (blue) and coated with TOPO (light blue) or PEO (red), taken on fresh spots (560 nm, CW, 40mW cm^{-2}); (b) Relative PLQY, taken with increasing (solid lines) or decreasing (dashed lines) excitation intensities (CW illumination, 560 nm, hold time between data points ~ 30 seconds) of MAPbI_3 thin films bare (dark blue) and coated with TOPO (light blue) or PEO (red); (c) Current density voltage (J - V) curves measured under 1 sun of MAPbI_3 devices with and without PEO interlayers; (d) open-circuit voltage (V_{oc}) transient measured from solar cells with and without PEO interlayers under one sun illumination.

4 Wide Band Gap perovskite – quantifying open-circuit voltage loss

Perovskites are particularly attractive materials for making multi-junction solar cells because their bandgap can be tuned across the visible spectrum simply by ionic substitution and mixing over a wide stoichiometric range. For ABX_3 perovskites, with the selection of $A = \text{Cs}$, methylammonium (MA^+) or formamidinium (FA^+), $B = \text{Sn}^{2+}$ or Pb^{2+} , and $X = \text{I}^-$, Br^- or Cl^- , the bandgap can be tuned from $\sim 1.24\text{eV}$ to 3.5eV . Mixed-halide I-Br perovskites, $\text{APb}(\text{I}_x\text{Br}_{1-x})_3$, have bandgaps between $1.48\text{-}2.35\text{eV}$, making them ideal for tandem and triple junction applications. However, the same ion-interchangeability that facilitates such convenient bandgap tuning also gives rise to a host of problems due to ionic diffusion. Notably, under illumination, “halide segregation” occurs in $\text{APb}(\text{I}_x\text{Br}_{1-x})_3$ films, leading to the formation of iodide-rich phases which have lower bandgaps than the surrounding unsegregated material. This was first observed through photoluminescence (PL) spectra in mixed-halide films, where a lower energy emission was correlated with

the formation of iodide-rich domains. Much work has since followed up on this phenomenon in an attempt to understand the mechanism. Notably, some studies have shown that enhanced crystallinity in the perovskite film can lead to reduced severity of the halide segregation.

The most efficient single junction perovskite solar cells reported to-date have bandgaps which range from 1.53 to 1.62 eV, and are generally composed of iodide-rich mixed-cation lead mixed-halide perovskites. These cells only have a loss in V_{OC} of ~ 60 mV from the theoretical limit (herein, we will refer to these “benchmark” perovskite cells as the ~ 1.6 eV gap cells). In contrast, the best mixed-halide devices with a high bromide content of 40% and above, show many hundreds of mV of loss in V_{OC} from the theoretical limit. The open-circuit voltage (V_{OC}) has been observed to “plateau” at about 1.2 V, (or even decrease) with the addition of Br to the $APb(I_{1-x}Br_x)_3$ perovskite, once the bromide content exceeds around 20%. The prevailing notion in the scientific community is that the emergence of the low energy PL peak in mixed-halide perovskite films corresponds to a limitation upon the open-circuit voltage; the open-circuit voltage will be “pinned” by the low bandgap iodide-rich impurity phases. However, intuition aside, there is yet no quantitative analysis of how halide segregation influences open-circuit voltage. Notably, the wide bandgap cell contributes the majority of the power output of a tandem cell. Thus, both scientifically and commercially, it is important to be able to quantify the loss occurring due to halide-segregation.

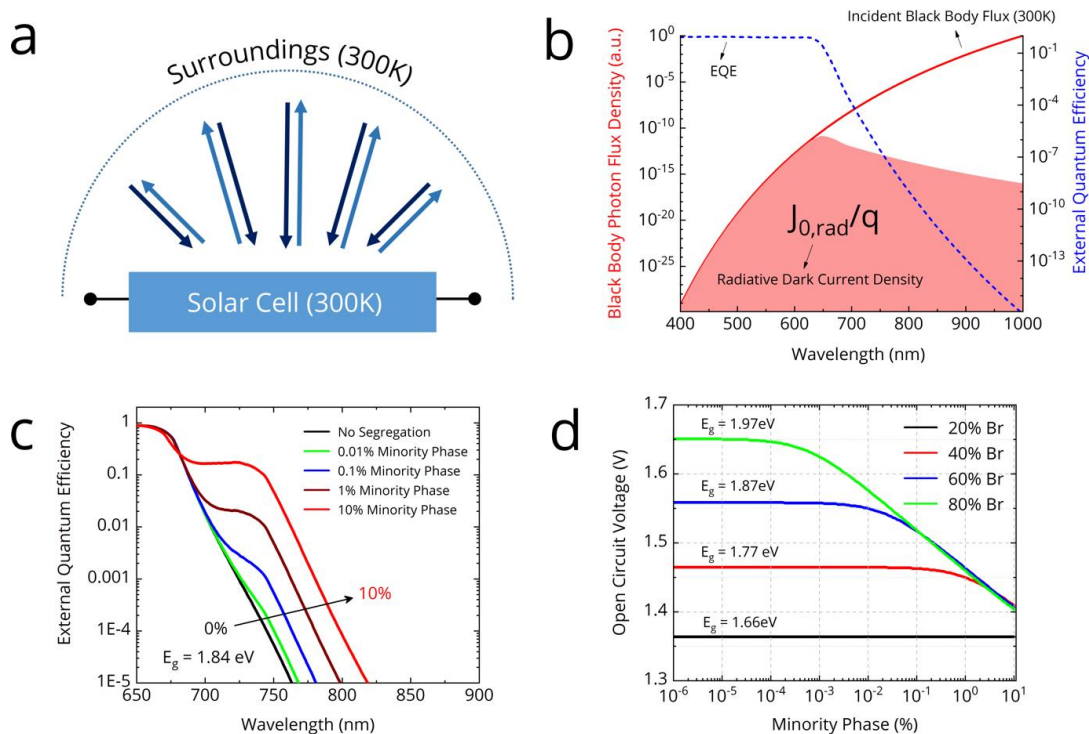


Figure 11. (a) Principle of Detailed Balance: In equilibrium, the black-body photon flux emitted and absorbed by the solar cell are equal. (b) The dark current J_0 is determined by the overlap integral of the blackbody flux and the EQE_{PV} . (c) Modelled EQE_{PV} for a halide segregating 1.84eV gap perovskite. The “bump” in the tail is due to absorption by the minority phase (80:20 I:Br) (d) Radiative limit V_{OC} as a function of the volume percentage of the minority phase (80:20 I:Br).

We begin by summarizing the factors that influence the open-circuit voltage of a solar cell and illustrate how we would expect the open-circuit voltage to evolve with the emergence of lower bandgap impurity phases. The mentioned equations have already been derived in the chapter *Thermodynamics and Optical Modelling*. We briefly review the ideas again to establish context. The open-circuit voltage of an ideal solar cell is expressed by the well-known relation:

$$V_{oc} = \frac{k_B T}{q} \ln \left(\frac{J_{sc}}{J_0} \right) \quad 10.1$$

Here, J_{sc} is the short circuit current density and J_0 is the dark recombination current density, also called as the dark current or reverse saturation current density. The calculation of J_{sc} via an overlap integral between the photovoltaic external quantum efficiency EQE_{PV} and the solar photon flux $\phi_{AM1.5}$ is well known:

$$J_{sc} = q \int_0^\infty EQE_{PV}(\lambda) \cdot \phi_{AM1.5}(\lambda) \cdot d\lambda \quad 10.2$$

The photovoltaic external quantum efficiency EQE_{PV} is defined as the fraction of photons incident on the solar cell that produce electric current. However, the calculation of the recombination current density J_0 is not often discussed, despite being theoretically well established. Experimentally, the dark recombination current density J_0 is the current that can be extracted from a solar cell in the dark by applying a large reverse bias. This current arises from thermally excited charges, i.e. charges excited by the ambient blackbody radiation being absorbed by the cell (Fig. 10.1a). This is the reason for J_0 being strongly dependent on junction temperature ($\propto T^3 e^{\frac{qE_g}{kT}}$).

In a real cell which includes non-radiative recombination, the recombination current J_0 is the sum of the radiative and the non-radiative recombination currents. The radiative recombination current can be calculated by using the principle of detailed balance: in equilibrium, the absorbed photon current must equal the emitted photon current. Thus, we can calculate the radiative recombination current through the overlap integral between the blackbody flux and the EQE_{PV} of the photoactive material. Thus, $J_{0,rad}$, which is equal to the emitted photon current can be written as:

$$J_{0,rad} = q \int_0^\infty \phi_{BB}(\lambda) \cdot EQE_{PV}(\lambda) \cdot d\lambda \quad 1$$

However, in a real cell, only a fraction of the recombination is radiative. The non-radiative recombination current is accounted for using the external electroluminescence quantum efficiency (EQE_{EL}), which is defined as the ratio of the radiative recombination current to the total recombination current (Equation 10.4). By definition, EQE_{EL} is always positive and less than unity.

$$EQE_{EL} = \frac{J_{0,rad}}{J_0} = \frac{J_{0,rad}}{J_{0,rad} + J_{0,non-rad}} \quad 2$$

U. Rau has rigorously established the relation between the open-circuit voltage and EQE_{EL} . Thus, by definition, the total recombination current density J_0 can be calculated by including the external electroluminescence quantum efficiency EQE_{EL} as a scaling factor:

$$J_0 = \frac{J_{0,rad}}{EQE_{EL}} = \frac{q}{EQE_{EL}} \int_0^\infty \phi_{BB}(\lambda) \cdot EQE_{PV}(\lambda) \cdot d\lambda \quad 3$$

Thus, J_0 can be calculated for a cell if EQE_{PV} , EQE_{EL} and the junction temperature are known. The relation between V_{OC} and EQE_{EL} can also be written as:

$$V_{oc} = V_{oc,rad} + \left(\frac{k_B T}{q}\right) \cdot \ln(EQE_{EL}) \quad 4$$

Here, $V_{oc,rad}$ is the V_{oc} calculated in the radiative limit. It is worth noting that because the black-body photon flux increases exponentially towards lower energies, tail state absorption makes the largest contribution to J_0 . In fact, the magnitude of J_0 is almost exclusively dictated by the position of the absorption tail. Thus, even small increases in tail-state absorption can increase J_0 by orders of magnitude, lowering V_{oc} (cf. equation 11). These tail states could even be so small as to be virtually invisible to conventional UV-Vis absorption spectroscopy or EQE_{PV} measurements. Consequently, their impact on J_{sc} would be negligible. However, their impact on the V_{oc} would be significant. This fact is central to the understanding of how the presence of low-bandgap phases affects V_{oc} .

The presence of a low-bandgap minority phase in the perovskite film can be expected to show up as a “bump” in the sub-bandgap absorptance. The magnitude of the absorption feature would be determined by the fraction of the film converted to the minority phase. As we have explained above, even a small below bandgap absorption feature would be sufficient to increase J_0 significantly. If the feature is sufficiently large, J_0 (and hence V_{oc}) would be completely determined by the minority phase, independent of the bandgap of the majority phase. This is the thermodynamic reasoning behind the assumption that voltage “pinning” will occur in cells exhibiting halide segregation. We used a generalized transfer matrix based optical model and detailed balance calculations to model the impact of halide segregation on V_{oc} in the radiative limit. The model serves to reveal the susceptibility of different compositions to V_{oc} losses upon halide segregation. We fixed the minority phase bandgap at 1.66 eV, consistent with reports of minority phase composition being 20:80 Br:I, regardless of majority phase bandgap. We modelled the complex refractive index of the perovskite as a Bruggeman effective medium of the minority and majority phases. We then used the generalized transfer matrix method to calculate the cell EQE_{PV} in an ITO/SnO₂/perovskite/spiro-OMeTAD/gold stack. Our modelled EQE_{PV} curves show a “bump” in the sub-gap absorption whose magnitude increases with fraction of minority phase (Fig. 11.c). We then employed detailed balance calculations to estimate the V_{oc} in the radiative limit as a function of percentage of minority phase in the film (Fig. 11.d).

Our model reveals that V_{oc} drops off logarithmically once the minority phase fraction exceeds a threshold. This threshold is smaller for larger bromide concentrations. For instance, an 80:20 Br:I film with 0.01% minority phase, incurs a voltage penalty of 76mV. However, a 40:60 Br:I film will show almost no V_{oc} loss at the same minority phase percentage. At higher minority phase concentrations (>1%), the V_{oc} is similar (“pinned”) for all majority phase compositions, but notably still around 70 mV larger than the V_{oc} generated from a 100% minority phase composition cell.

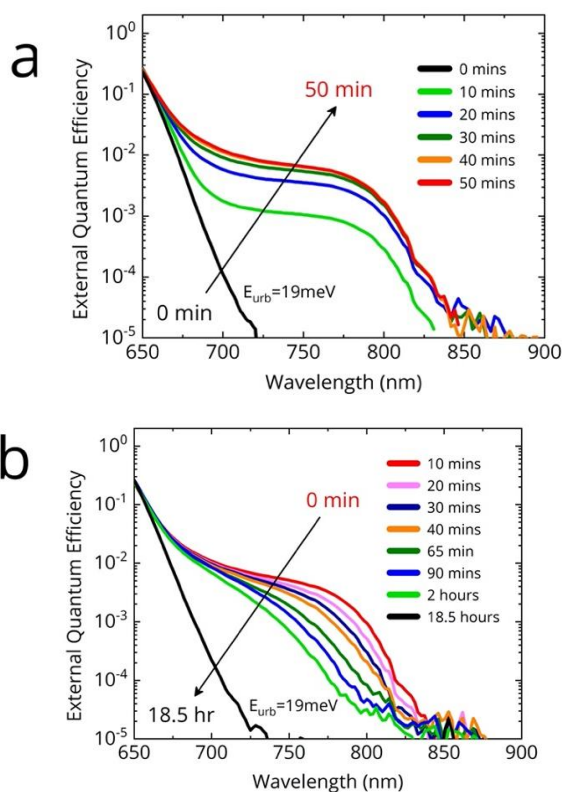


Figure 12 | Photovoltaic External Quantum Efficiency (EQE_{PV}) of a $FA_{0.83}MA_{0.17}Pb(I_{0.4}Br_{0.6})_3$ cell measured with Fourier Transform Photocurrent Spectroscopy (FTPS). **(a)** Time evolution of EQE_{PV} under simulated AM1.5 illumination. **(b)** Time evolution of EQE_{PV} upon being kept in the dark.

We used Fourier Transform Photocurrent Spectroscopy (FTPS) to study the effect of simulated sunlight on the external quantum efficiency of an $FA_{0.83}MA_{0.17}Pb(I_{0.4}Br_{0.6})_3$ solar cell deposited via the anti-solvent quenching method. In figure 10.2a we show the time-evolution of the External Quantum Efficiency (EQE_{PV}) spectrum of an $FA_{0.83}MA_{0.17}Pb(I_{0.4}Br_{0.6})_3$ device under simulated AM1.5 illumination. We use simulated AM1.5 illumination as phase segregation has been shown to be sensitive to illumination spectrum and intensity. We held the cells at open-circuit at all times. After 10 minutes of light soaking, we observe a new shoulder at ~ 780 nm (1.59 eV) in the sub-bandgap region of the EQE_{PV} spectrum, consistent with the photo-induced formation of iodide-rich impurity phases. We observe this feature to grow, and eventually saturate at about 1% quantum efficiency after 40 minutes. At saturation, the absorption edge of the feature is approximately 800 nm (1.55 eV), as determined from the EQE_{PV} inflection point. We identify this feature as absorption from the iodide-rich regions formed upon illumination (we note that the A site composition is FA-rich, and hence lower bandgap than $MAPbX_3$ perovskites). We shall henceforth refer to the iodide-rich regions as the *minority phase*, and the phase in which the minority phase is embedded as the *majority phase*. The appearance of the minority phase causes virtually no change in the bandgap of the majority phase, and is hence virtually invisible to conventional UV-Vis absorption spectroscopy. Consequently, the photo-induced carrier generation rate in the cell is unaffected. Upon being kept in dark, we observe the feature to relax back towards the

original starting point, albeit much more slowly over more than 18 hours (Fig. 12.b). Incidentally, upon halide “de-segregation”, the minority phase appears to progressively become less rich in iodide. This is in contrast to segregation, where the heavily iodide-rich phase rapidly forms first. We interpret this to imply that halide segregation proceeds by first nucleating the lowest-bandgap phase, followed by the growth of this phase. In contrast, during desegregation, the iodide-rich phase absorption gradually blue shifts, while also reducing in intensity. This suggests that the mechanism of desegregation is likely to be entropic mixing, which causes the minority phase to be slowly enriched with bromide, consistent with disappearance of the most iodide-rich phases first.

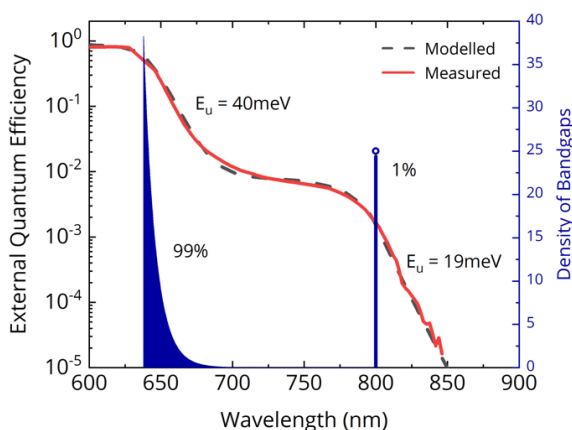


Figure 13 | (a) Modelled halide segregated EQE_{PV} (dotted green) and the distribution of bandgaps in perovskite (blue) at saturated halide segregation.

Studies so far treat halide segregation as a simple two phase phenomenon. A minority phase of a single composition (often 20:80 Br:I) is assumed to have formed, which is the source of the low-energy photoluminescence peak. In practice, such a clear-cut phase separation is unlikely. A continuum in iodide concentration, or at least multiple phases are more probable. Our FTPS measurements (Fig. 13) confirm this hypothesis. The absorption edge of the pristine cell has an Urbach energy of 19 meV. As the film segregates, we estimate the Urbach energy of the majority phase to increase, reaching 40 meV after 50 minutes of light soaking. This points to considerable compositional inhomogeneity in the majority phase due to segregation. Serious V_{OC} losses are expected when the Urbach energy exceeds $k_B T$. This loss mechanism in halide segregated films has hitherto escaped attention. However, the most significant losses do arise from the iodide-rich minority phase. The appearance of a nearly flat shoulder between 725-800 nm indicates that the minority phase is comprised of material with a narrow bandgap range centered on 1.55 eV. The Urbach energy of the tail is 19 meV—similar to that of the unsegregated film, but notably slightly larger than the ~15 meV expected for $FA_{0.83}MA_{0.17}PbI_3$.

We model the halide segregated EQE_{PV} (Fig. 12.a; red curve at 50mins) using the generalized transfer matrix method and effective medium approximation, and use it to extract the distribution of bandgaps in the material. We find that the majority phase exhibits an exponential distribution of bandgaps, decaying from a peak at 640 nm. The

minority phase has a single bandgap at 800 nm. Through our model, we estimate that the minority phase occupies about 1 % by volume of the film (assuming the optical density scales with thickness). This is in agreement with previous estimation at 1% by Hoke et al. The extent of segregation can also be roughly estimated from the EQE_{PV} , by observing the magnitude of the minority phase absorption, which is also 1%. This follows from Lambert's law, since EQE_{PV} scales linearly with absorptance at low-absorptance ($\ll 1$).

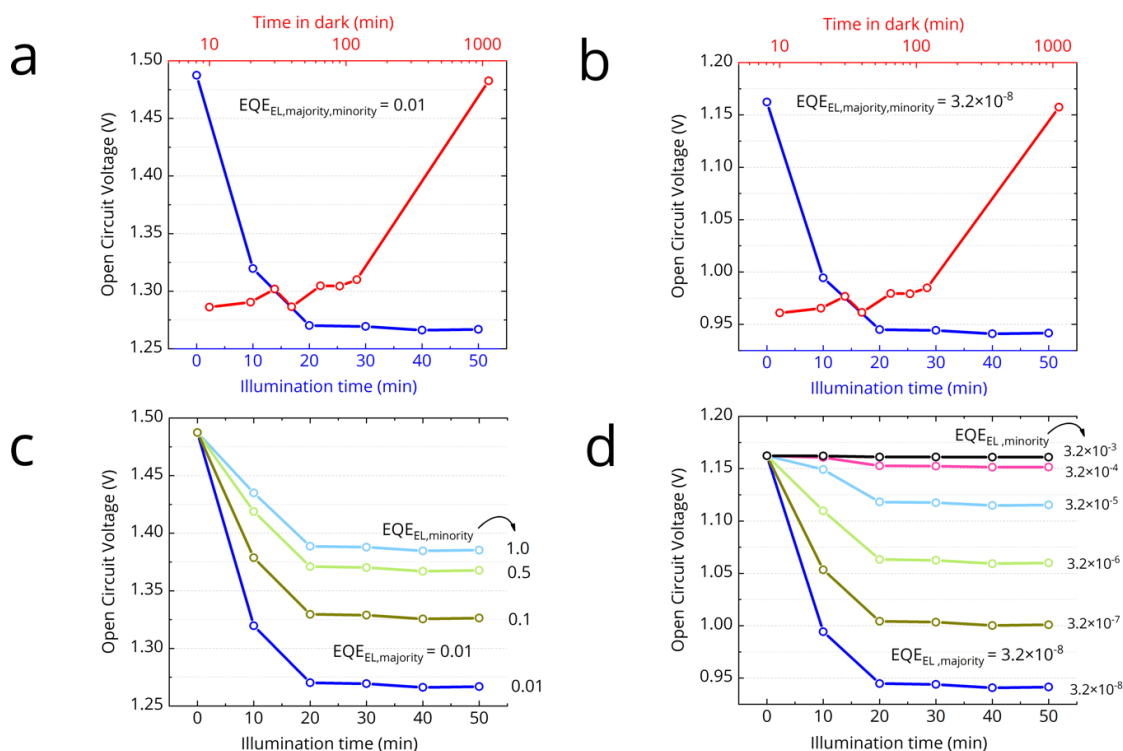


Figure 14 | Time evolution of V_{OC} calculated via detailed balance using the FTPS data measured on $FA_{0.83}MA_{0.17}Pb(I_{0.4}Br_{0.6})_3$ based cells. We show the effect of varying the EQE_{EL} of the two phases. **(a)** Time evolution of V_{OC} , assuming $EQE_{EL} = 0.01$ for both the majority and minority phases. This would be the voltage of a wide bandgap cell if it were electronically as good as the best 1.6 eV cells. **(b)** Time evolution of V_{OC} , assuming a realistic $EQE_{EL} = 3.2 \cdot 10^{-8}$ for both the majority and minority phases. **(c)** Time evolution of V_{OC} for a range of minority phase EQE_{EL} , fixing majority phase $EQE_{EL} = 0.01$. **(d)** Time evolution of V_{OC} for a range of minority phase EQE_{EL} , fixing majority phase $EQE_{EL} = 3.2 \cdot 10^{-8}$.

The severity of halide-segregation in a solar cell is best characterized by the accompanying V_{OC} loss. Here, we perform detailed balance calculations on the presented FTPS data to determine the expected loss in V_{OC} arising from halide-segregation. This calculated loss can be used as a measure of the severity of halide-segregation in a cell. We perform the previously described detailed balance calculations (Equations 1-4) on the measured time dependent EQE_{PV} spectra (Fig. 12.a, 12.b) to get the expected time dependence of the open-circuit voltage (Fig. 14). In the first instance, we assume that both the majority and minority phase have the same time-invariant radiative efficiency, EQE_{EL} (expressed as a fraction of unity, where $EQE_{EL} = 1$ is 100%). The magnitude of the voltage loss arising from halide segregation is not dependent on the choice of EQE_{EL} , as long it does not vary with time. So its precise value is not relevant. Later, we also discuss the case of the two phases having different EQE_{EL} .

The best perovskite cells (with a bandgap of $\sim 1.6\text{eV}$) today typically have an $\text{EQE}_{\text{EL}} \sim 0.01$. We set $\text{EQE}_{\text{EL}} = 0.01$ for both the minority and majority phases and calculate the time evolution of V_{OC} (Fig. 14.b). We calculate $V_{\text{OC}} = 1.49\text{ eV}$ from the pristine cell. As segregation proceeds in time, we calculate that the V_{OC} should drop very rapidly in the beginning, losing 170 mV in 10 minutes, despite sub-bandgap EQE_{PV} being just $\sim 0.1\%$. After 20 minutes, we estimate the V_{OC} to have dropped by 220 mV and hit 1.27 V. After 20 minutes, we determine that the V_{OC} is stable at 1.27 V, despite an increasing sub-bandgap absorption. Thus, we estimate that the total V_{OC} loss at saturated segregation to be 220 mV. This loss is independent of the EQE_{EL} chosen, provided it does not change during time under illumination. Setting $\text{EQE}_{\text{EL}} = 3.2 \cdot 10^{-8}$ predicts a more realistic $V_{\text{OC}} = 1.16\text{ V}$ from pristine cell (Equation 10.5). The calculated V_{OC} loss due to segregation, however, remains the same at 220 mV (Fig. 14.b).

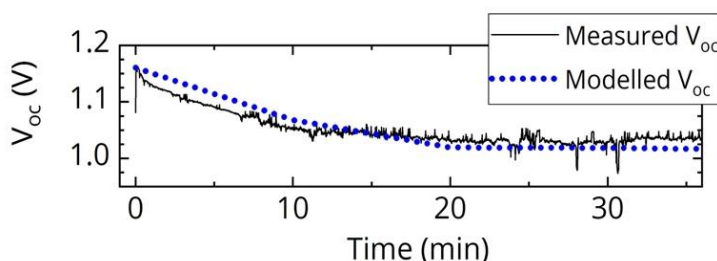


Figure 15 | Measured time evolution of the V_{OC} of a halide segregating cell (black). The modelled V_{OC} (dotted blue) allows us to extract $\text{EQE}_{\text{EL},\text{majority}} = 3.2 \cdot 10^{-8}$ and $\text{EQE}_{\text{EL},\text{minority}} = 6.2 \cdot 10^{-7}$.

Since the carrier diffusion length in these materials is relatively long, the charge carriers will explore a large volume of film under open-circuit conditions, when they are not being extracted. Therefore, they are likely to find the low bandgap minority phase regions, and will become localized within these regions due to energetic confinement. In a real cell, the minority phase occupies a small fraction of the total film volume. Since the emission from a halide-segregated film is predominantly via this lower energy phase, we know that there is a predominant accumulation of charge carriers in this region. This accumulation of carriers within the low bandgap regions of mixed phase perovskites, is often referred to as charge-funneling. The average carrier concentration within the minority phases, will therefore be much higher than in the majority phase regions (or non-segregated film). For a 1% segregated film, this may therefore result in a 100 fold increase in charge-carrier density within the low bandgap phase (in comparison to the charge density in the unsegregated majority phase). This increased charge density will promote radiative recombination, due to bimolecular radiative recombination competing more strongly with monomolecular non-radiative recombination. Trap filling from the local increase in carrier density will also serve to increase the radiative efficiency. This therefore suggests that we would expect an increased EQE_{EL} from the minority phase. We note that a narrower bandgap 3D minority phase inclusion in a wider bandgap 2D majority phase matrix, is the strategy adopted for the best perovskite light emitting diodes. In our case here, the increase in radiative efficiency of the iodide-rich minority phase, would cause the drop in V_{OC} to be less dramatic. Thus we expect that the 220 mV loss we estimate from the

EQE_{PV} measurements, is an upper-bound for the V_{OC} loss. We also calculate the V_{OC} (Fig. 14.c) by varying the EQE_{EL} of the minority phase, while keeping the majority phase EQE_{EL} fixed at 0.01. We find that every ten-fold increase in the radiative efficiency of the minority phase, the V_{OC} loss due to halide segregation reduces by $\sim 55\text{meV}$.

If we set the majority phase EQE_{EL} at a realistic $3.2 \cdot 10^{-8}$, we can vary minority phase EQE_{EL} by many more orders of magnitude (Fig. 14.d). When we choose the radiative recombination of the minority phase to be 100,000 times higher than the majority phase, then we estimate no V_{OC} loss following halide segregation. In this case, the recombination rate in the absorber would be controlled by fast non-radiative recombination in the majority phase, and the formation of a low-bandgap phase would only cause a negligible increase in the net recombination rate.

In order to understand the impact of the enhanced EQE_{EL} that we just described, we measure the time evolution of the open-circuit voltage of a pristine $FA_{0.83}MA_{0.17}Pb(I_{0.4}Br_{0.6})_3$ cell (bandgap 1.94eV) under simulated AM1.5 conditions (Fig. 10.5). We observe the voltage to drop quickly initially and then stabilize with a V_{OC} loss of around 120mV after 20 minutes. This is consistent with the behavior predicted by our EQE_{PV} measurements (Fig. 14). We model the curve using the approach previously presented (Fig. 15), and vary the EQE_{EL} of the majority and minority phase until we achieve a similar trend. We find consistency if we set the EQE_{EL} of the majority phase to $3.2 \cdot 10^{-8}$, and the EQE_{EL} of the minority phase to $6.2 \cdot 10^{-7}$. This suggests a 19-fold enhanced EQE_{EL} in the minority phase, as compared to the majority phase, which seems to be perfectly reasonable.

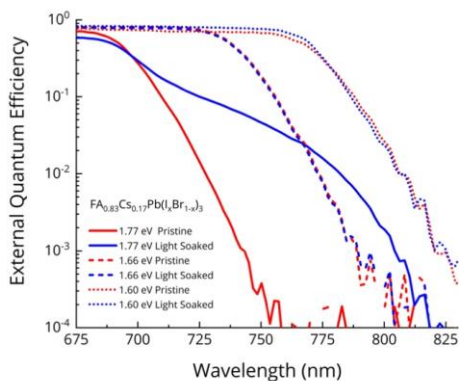


Figure 16 | Photovoltaic External Quantum Efficiencies (EQE_{PV}) of $FA_{0.83}Cs_{0.17}Pb(I_xBr_{1-x})_3$ based p - i - n solar cells measured before and after light soaking for 2 hours under 0.2 suns illumination.

In order to quantify the V_{OC} penalty from halide segregation, in the preceding sections we presented studies on a perovskite composition (FAMA based) and bandgap (1.94 eV) that rapidly underwent halide segregation, in order to exemplify our theoretical assessment. However, in order to exemplify more state-of-the-art wide bandgap compositions, we now present results for the $FA_{0.83}Cs_{0.17}Pb(I_xBr_{1-x})_3$ family. We fabricated $FA_{0.83}Cs_{0.17}Pb(I_xBr_{1-x})_3$ based p - i - n devices of three different bandgaps: 1.77

eV (40% Br, suitable for perovskite-perovskite tandems), 1.66 eV (23% Br, ideal for perovskite-silicon tandems), and 1.60 eV (10% Br, best bandgap for single-junction performance in our lab). We light soaked the devices for two hours under 1 sun simulated AM1.5 illumination, till the absorption tail was seen to evolve no more, and show the measured FTPS-EQE_{PV} spectra for the pristine and light-soaked devices.

The 1.66 eV and 1.60 eV absorbers show negligible changes in the absorption tail, indicating that the low bandgap phase segregated fraction is less than our resolution limit of 10^{-4} . As our modelling (Fig. 10.d) has indicated, this will be accompanied by negligible V_{OC} loss. Furthermore, the Urbach energy, which is a measure of electronic disorder, is just 15 meV before and after segregation, suggesting that no segregation has occurred. The 1.77 eV bandgap absorber (40% Br), on the other hand, undergoes halide-segregation, evolving a sub bandgap absorption feature. The formed absorption shoulder is also quite broad, suggesting that there is no single prominent composition, but only a mixture of phases. A detailed balance calculation on the EQE_{PV} of this 1.77eV cell, presented in Fig. 10.6, reveals a 97 mV V_{OC} penalty due to halide-segregation, assuming no change in the radiative efficiency EQE_{EL} during segregation. As we have already explained, we expect that the actual V_{OC} loss will be less than 97 mV, owing to increased radiative efficiency of the iodide-rich phase. Indeed, the V_{OC} measurement done simultaneously with the FTPS-EQE_{PV} reveals that the loss is only 75 mV, since the V_{OC} drops from 1.105 V to 1.030 V.

In the preceding sections, we combined sensitive EQE_{PV} measurements with detailed balance calculations to quantify the V_{OC} penalty due to halide segregation in FAMA and FACs based mixed-halide perovskite cells. In this section, we quantitatively compare the segregation-loss to the non-radiative V_{OC} loss.

In our FAMA based 1.94eV bandgap cell, we calculated the expected V_{OC} to be 1.61 V in the radiative limit. Our cell shows a V_{OC} , prior to halide segregation, of 1.16 V, suggesting an initial EQE_{EL} $\sim 10^{-8}$. The situation is similar in our FACs based 1.77 eV bandgap device, which in the radiative limit would deliver a 1.49 V V_{OC} . However, the device exhibits a V_{OC} , prior to halide segregation of 1.105 V, suggesting an initial EQE_{EL} $\sim 10^{-6}$. The non-radiative V_{OC} loss in this instance (385 mV) is over five times the segregation loss (75mV). Clearly, the V_{OC} loss due to non-radiative recombination is much more overwhelming than the loss from segregation. In comparison, the best perovskite cells (~ 1.6 eV) have non-radiative losses of approximately 60 mV. If this is achieved for 1.94 and 1.77 eV bandgap cells, they would deliver a V_{OC} of 1.54 and 1.43 V respectively, prior to halide segregation. Hence, even if halide segregation occurred, and induced a voltage penalty to the same extent that we have measured here, we would still reach open-circuit voltages of 1.42 V and 1.33 V for the 1.94 eV and 1.77 eV bandgap cells respectively.

Therefore, the performance of mixed-halide perovskites is predominantly limited by trap-assisted non-radiative recombination and not halide-segregation. The problem in mixed-halide perovskites seems to be two-fold: a) non-radiative recombination within the perovskite absorber and b) Interfacial non-radiative recombination at the perovskite/charge extraction layer heterojunctions. In our 1.77 eV bandgap FACs based devices, the Urbach energy, which represents electronic disorder in the continuum of

states, is low at only 15meV. This indicates that the poor quality does not arise from electronic disorder in the bands. We measure a PLQE of approximately 0.3% for the isolated perovskite film on glass. In comparison, the PLQE of the best metal halide perovskite films (~1.6 eV bandgap) is over 10%. Therefore, efforts are required to minimise the defects responsible for non-radiative recombination in these wider band gap mixed-halide perovskites. A further significant loss occurs due to the poor electronic quality of the perovskite/charge-transport-layer heterojunctions. Considering the difference between the inferred EQE_{EL} (10^{-6}) and the PLQE of the isolated perovskite film (10^{-3}), we infer that the contact materials quench the PLQE by three orders of magnitude. From this perspective, the electron-transport layer Phenyl-C61-butyric acid methyl ester (PCBM) is particularly deleterious, since it significantly quenches the PLQE of our 1.77 eV gap perovskite films to below our detector limit (0.01%). By considering these absolute radiative efficiency values, we can estimate that the non-radiative losses from within the 1.77 eV gap perovskite absorber are responsible for ~180 mV loss in V_{oc} , and the integration into the device induces a further ~180 mV loss, with the latter primarily governed by the charge extraction layer/perovskite heterojunctions.

Thus, as a first priority, improved transport layers have to be identified by a systematic study of PL quenching, using the approach demonstrated by Stolterfoht. M. et al. The development of new transport layers with new doping strategies to enable better band alignment, is also essential. Efforts to optimise the crystallisation and passivation of defects are also needed to eventually bring the PLQE of wide bandgap films on par with the best 1.6 eV bandgap films (~10%).

As a final note, halide segregation has itself been found to correlate positively with the fraction of non-radiative recombination in the film. In addition, halide segregation has been shown to be highly suppressed in perovskite films with lower trap densities. We may therefore postulate that it is the accumulated trapped charge which offers the electrostatic driving force for halide-segregation. We therefore expect that the route to maximise the radiative efficiency via reducing the trap density in the mixed-halide perovskites will not only maximise the initial V_{oc} , but will also likely overcome halide segregation itself.

In conclusion, we have quantified the impact of halide-segregation upon the open-circuit voltage (V_{oc}) of mixed-halide perovskite solar cells, using Fourier-Transform Photocurrent Spectroscopy (FTPS) measurements coupled with detailed balance calculations. Our results reveal that the V_{oc} loss from non-radiative recombination (~400 mV) is four to five times the loss from halide-segregation (~100 mV) in both FAMA (1.94 eV) and FACs (1.77 eV) based solar cells. These results represent the first quantitative evaluation of the contribution of halide-segregation towards the poor performance of mixed-halide perovskite cells. We suggest that currently, the performance of mixed-halide cells is limited by poor electronic quality of the perovskite cell which results in a low radiative efficiency, and not by halide segregation. The cause of this low radiative efficiency is twofold: a) perovskite absorber with a high degree of trap assisted non-radiative recombination and b) poor electronic quality of perovskite/charge-transport-layer heterojunctions, leading to “heterojunction-induced” non-radiative losses.

To reach higher open-circuit voltages, improving the radiative efficiencies of mixed-halide perovskite films, and developing more efficient perovskite/charge extraction layer interfaces should be viewed as a matter of priority. With such improved materials processing, we suggest that a V_{OC} of up to 1.33 V is within reach for a 1.77 eV perovskite, even if halide segregation remains unsuppressed. Our work clearly highlights that the means to solve the voltage deficit issue in wide band gap mixed-halide cells, is to focus on reducing the initial defect density, and to neglect halide segregation as an issue, until improved radiative efficiency has been achieved. We also suggest that future studies on mixed-halide perovskites should include sensitive EQE_{PV} measurements coupled with detailed balance calculations to clearly differentiate V_{OC} loss due to halide-segregation and non-radiative recombination.

5 Conclusions

Pristine, bilayers and complete devices (1.65eV and wide bandgaps metal halide perovskite thin films) have been investigated in order to identify possible electronic losses in solar cells. In particular the role of bulk and surface defects has been elucidated and passivation strategies have been proposed.